Supplementary Figures

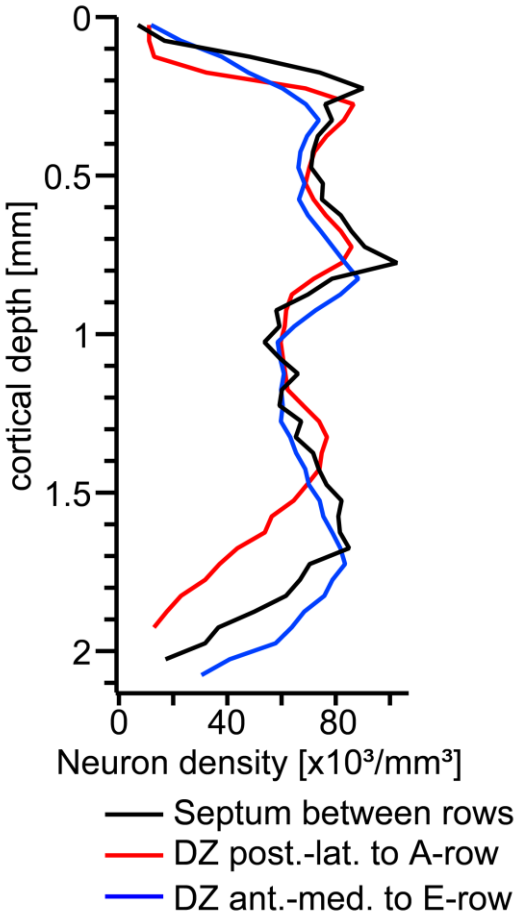

Figure S1: Neuron distributions in septa between whisker rows are indistinguishable from dysgranular zones surrounding rat vibrissal cortex. Average vertical neuron density profiles measured exclusively in the septum between rows (black; 2x between C- and D-rows, 1x between D- and E-rows), the dysgranular zone posterior-lateral to the A-row (red) and anterior-medial to the E-row (blue).

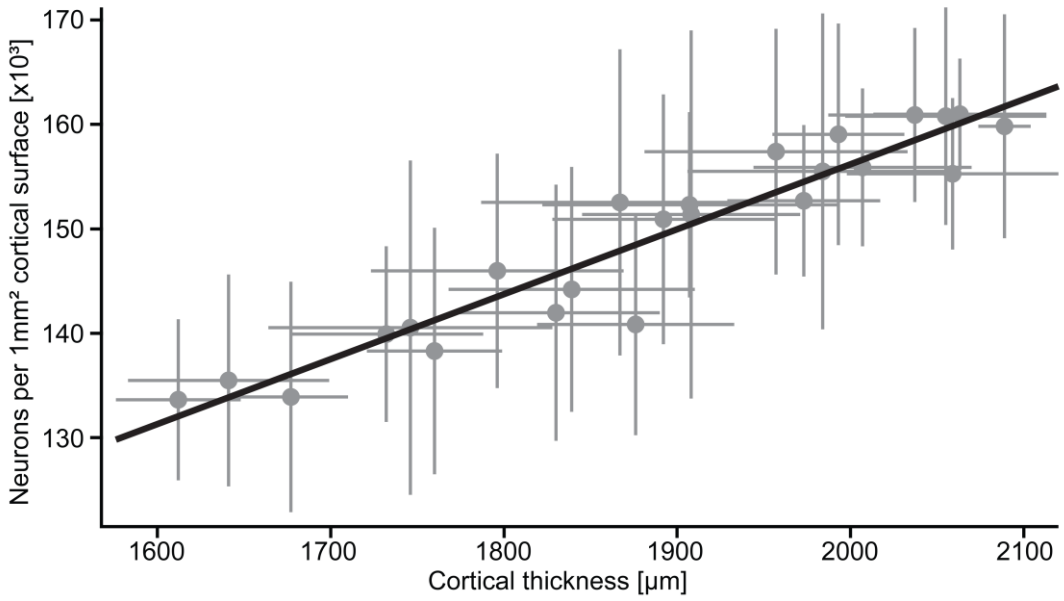

Figure S2: Changes in cortical thickness are not compensated by neuron densities as suggested by 'structural uniformity'. Average number of neurons underneath 1mm² of cortical surface as a function of cortical thickness. Calculated for individual barrel columns by dividing the average number of neurons inside the barrel columns by the average cross-sectional area of the barrel column. Cortical thickness is the pia-WM distance measured along the vertical column axis. Pearson's correlation coefficient: $r=0.95$, $p<0.0001$ (two-sided t-test). Error bars are ±1 SD.

Supplementary Tables

Supplementary Table 1: Across-animal-variability in cellular organization of rat vibrissal cortex (S1) and thalamus (VPM).

α-δ, A1-E4	Cortex	SD (%)	Thalamus	SD (%)
neurons	529,715 ± 39,104	7	9,963 ± 718	7
excitatory	460,981 ± 51,583	11	9,963 ± 718	7
inhibitory	68,734 ± 14,160	21		
columns	430,980 ± 36,830	9	6,225 ± 173	3
septa	98,735 ± 10,907	11	3,735 ± 657	18
volume (mm^3)	6.60 ± 0.58	9	0.19 ± 0.03	16
columns	5.24 ± 0.51	10	0.12 ± 0.01	8
septa	1.36 ± 0.16	12	0.07 ± 0.02	29
density (mm^{-3})	80,419 ± 3,688	5	52,494 ± 5,082	10
columns	82,402 ± 4,011	5	51,507 ± 4,422	9
septa	72,792 ± 2,419	3	54,440 ± 6,559	12
DZ*/RT	68,236 ± 2,226	3	49,680 ± 1,097	2
DZ$^{\$}$/POm	66,311 ± 1,084	2	41,477 ± 3,612	9

All numbers are mean ± SD (S1: n=4, VPM: n=3). *denotes density in DZ anterior-medial to the E-row in vibrissal cortex; n=2. $^{\$}$denotes density in DZ posterior-lateral to the A-row in vibrissal cortex; n=3.

Supplementary Table 2: Cellular composition of Layer 1 (L1).

	L1-L2/3 border [µm]	L1 neurons	L1 exc. neurons	L1 inh. neurons	L1 fraction [%]
α	139 ± 20	56 ± 27	32 ± 19	23 ± 18	0.5
β	143 ± 13	55 ± 15	22 ± 6	32 ± 15	0.4
γ	151 ± 17	85 ± 22	37 ± 16	48 ± 11	0.4
δ	152 ± 9	94 ± 38	46 ± 25	48 ± 23	0.4
A1	140 ± 11	58 ± 36	43 ± 36	15 ± 9	0.5
A2	137 ± 8	103 ± 131	81 ± 121	22 ± 12	0.8
A3	147 ± 21	74 ± 62	43 ± 76	31 ± 18	0.8
A4	154 ± 22	55 ± 35	24 ± 17	31 ± 25	0.6
A-row	145 ± 8	72 ± 22	48 ± 24	25 ± 8	0.6 ± 0.2
B1	139 ± 10	94 ± 22	58 ± 10	37 ± 18	0.7
B2	140 ± 17	101 ± 52	74 ± 51	27 ± 7	0.7
B3	145 ± 21	69 ± 54	48 ± 55	21 ± 8	0.5
B4	151 ± 20	63 ± 29	38 ± 33	25 ± 9	0.5
B-row	144 ± 5	82 ± 19	54 ± 15	27 ± 7	0.6 ± 0.1
C1	139 ± 17	68 ± 10	29 ± 12	39 ± 13	0.4
C2	157 ± 14	142 ± 42	91 ± 41	51 ± 17	0.7
C3	154 ± 15	95 ± 24	58 ± 30	37 ± 12	0.6
C4	158 ± 8	60 ± 30	34 ± 18	25 ± 19	0.4
C-row	152 ± 9	91 ± 37	53 ± 28	38 ± 11	0.5 ± 0.2
D1	154 ± 19	90 ± 11	42 ± 18	48 ± 13	0.4
D2	157 ± 16	128 ± 25	64 ± 2	64 ± 27	0.6
D3	159 ± 14	149 ± 37	83 ± 28	66 ± 42	0.7
D4	161 ± 26	105 ± 49	67 ± 48	38 ± 19	0.5
D-row	158 ± 3	118 ± 26	64 ± 17	54 ± 13	0.5 ± 0.1
E1	158 ± 7	123 ± 20	63 ± 21	60 ± 15	0.5
E2	160 ± 11	153 ± 37	86 ± 38	67 ± 15	0.5
E3	159 ± 15	148 ± 47	90 ± 34	58 ± 20	0.5
E4	155 ± 23	171 ± 60	114 ± 52	57 ± 13	0.7
E-row	158 ± 2	149 ± 20	88 ± 21	60 ± 5	0.6 ± 0.1
Average	150 ± 8	97 ± 36	57 ± 25	40 ± 16	0.5 ± 0.1

Fraction: relative to average total number of neurons in the same column. Layer borders were determined using previously determined cell type-specific vertical extents (1). Specifically, the border of L4 spiny stellate neurons coincided with the GAD67-based definition of the respective barrel top and bottom, as well as with the excitatory neuron density peak (Gaussian approximation ± full width half maximum; see (2)). Thus, the L2/3-L4 as well as the L4-L5 borders were consistent across cytoarchitectonic-, cell type- and neuron density-based definitions. The remaining layer borders were determined for each barrel column individually using linear interpolations of cell type borders determined for the D2 barrel column. Interpolations were performed between the pia and respective barrel top, and between the barrel bottom and respective WM for each barrel column individually. Within the first ~100µm below the pia, virtually all neurons are inhibitory, as reported previously (3). The depth location of the first excitatory neurons below the pia surface may thus be used as an alternative definition of the L1/2 layer border (3), compared to the cell type borders (~150µm) (1) used in the present study.

Supplementary Table 3: Cellular composition of Layer 2/3 (L2/3).

	L2/3-L4 border [µm]	L2/3 neurons	L2/3 exc. neurons	L2/3 inh. neurons	L2/3 fraction [%]
α	509 ± 72	2,958 ± 989	2,663 ± 935	295 ± 90	24.9
β	523 ± 48	3,580 ± 457	3,221 ± 429	359 ± 100	23.9
γ	552 ± 62	4,899 ± 219	4,429 ± 239	470 ± 141	25.1
δ	555 ± 33	5,026 ± 319	4,560 ± 227	466 ± 93	23.0
A1	513 ± 39	2,977 ± 891	2,294 ± 542	310 ± 148	24.8
A2	502 ± 28	2,743 ± 680	2,067 ± 281	365 ± 204	22.9
A3	540 ± 78	2,339 ± 459	1,894 ± 214	279 ± 178	24.2
A4	564 ± 79	2,509 ± 829	2,187 ± 673	322 ± 200	25.7
A-row	530 ± 28	2,642 ± 278	2,110 ± 171	319 ± 35	24.4 ± 1.2
B1	508 ± 37	3,296 ± 269	2,922 ± 311	374 ± 105	23.1
B2	512 ± 61	3,404 ± 1,044	2,568 ± 579	356 ± 92	23.1
B3	531 ± 77	2,918 ± 1,038	2,100 ± 437	326 ± 116	22.1
B4	552 ± 73	2,797 ± 681	2,496 ± 665	301 ± 77	22.4
B-row	526 ± 20	3,104 ± 292	2,522 ± 337	339 ± 33	22.7 ± 0.5
C1	511 ± 63	3,869 ± 564	3,464 ± 630	405 ± 92	22.3
C2	576 ± 52	4,758 ± 358	4,273 ± 445	485 ± 140	24.2
C3	564 ± 54	3,887 ± 902	3,455 ± 903	432 ± 37	22.0
C4	580 ± 30	3,424 ± 622	3,099 ± 650	326 ± 31	23.1
C-row	558 ± 32	3,984 ± 558	3,573 ± 497	412 ± 67	22.9 ± 1.0
D1	564 ± 71	4,717 ± 1,109	4,268 ± 1,123	450 ± 128	23.3
D2	575 ± 57	5,458 ± 351	4,936 ± 421	522 ± 99	23.4
D3	582 ± 51	5,117 ± 947	4,609 ± 1,021	508 ± 85	22.4
D4	589 ± 97	4,927 ± 977	4,439 ± 1,045	488 ± 131	22.7
D-row	577 ± 11	5,055 ± 314	4,563 ± 285	492 ± 31	23.0 ± 0.5
E1	579 ± 26	5,839 ± 693	5,279 ± 741	560 ± 50	22.9
E2	584 ± 39	6,751 ± 1,097	6,107 ± 1,147	644 ± 54	22.8
E3	584 ± 55	6,164 ± 957	5,520 ± 969	644 ± 91	22.2
E4	569 ± 84	5,407 ± 1,604	4,852 ± 1,542	554 ± 93	21.6
E-row	579 ± 7	6,040 ± 566	5,439 ± 524	601 ± 50	22.4 ± 0.6
Average	551 ± 30	4,157 ± 1,267	3,654 ± 1,244	427 ± 109	23.3 ± 1.1

The inhibitory neuron distribution in rat vibrissal cortex (see Fig. 2D) is indicative of a separation of L2/3 into L2 (defined by high inhibitory neuron density) and L3 (defined by low inhibitory neuron density), as reported previously (3).

Supplementary Table 4: Cellular composition of Layer 4 (L4).

	L4-L5 border [µm]	L4 neurons	L4 exc. neurons	L4 inh. neurons	L4 fraction [%]
α	746 ± 35	2,674 ± 646	2,324 ± 606	350 ± 52	22.9
β	770 ± 46	3,645 ± 1,070	3,290 ± 1,061	354 ± 129	24.2
γ	794 ± 46	4,562 ± 1,134	4,117 ± 1,055	445 ± 251	23.0
δ	842 ± 36	5,227 ± 1,597	4,634 ± 1,630	592 ± 266	23.6
A1	749 ± 34	2,659 ± 645	2,328 ± 811	460 ± 117	22.8
A2	774 ± 32	3,027 ± 834	2,686 ± 1,029	390 ± 20	25.4
A3	802 ± 26	2,268 ± 664	2,063 ± 771	312 ± 40	23.2
A4	801 ± 30	2,072 ± 580	1,781 ± 517	291 ± 145	21.4
A-row	782 ± 25	2,506 ± 424	2,214 ± 386	363 ± 77	23.2 ± 1.7
B1	791 ± 46	3,856 ± 1,177	3,415 ± 1,206	441 ± 36	26.4
B2	810 ± 14	3,913 ± 923	3,647 ± 967	612 ± 263	27.2
B3	846 ± 33	3,407 ± 442	3,080 ± 576	463 ± 152	26.9
B4	834 ± 51	2,757 ± 232	2,369 ± 373	388 ± 147	22.6
B-row	820 ± 25	3,483 ± 534	3,128 ± 557	476 ± 96	25.8 ± 2.1
C1	820 ± 28	4,911 ± 1,264	4,462 ± 1,286	449 ± 199	27.8
C2	855 ± 25	4,756 ± 734	4,184 ± 859	572 ± 229	24.1
C3	896 ± 35	4,688 ± 587	4,105 ± 600	583 ± 145	26.9
C4	904 ± 47	3,900 ± 753	3,389 ± 717	511 ± 181	26.4
C-row	869 ± 39	4,564 ± 452	4,035 ± 457	529 ± 62	26.3 ± 1.6
D1	889 ± 40	5,363 ± 545	4,703 ± 959	660 ± 481	26.9
D2	900 ± 50	6,233 ± 796	5,391 ± 1,267	842 ± 588	26.6
D3	918 ± 45	6,006 ± 911	5,289 ± 1,100	717 ± 189	26.5
D4	934 ± 72	5,777 ± 269	5,066 ± 415	711 ± 435	26.8
D-row	910 ± 20	5,844 ± 371	5,112 ± 305	732 ± 77	26.7 ± 0.2
E1	864 ± 50	5,712 ± 1,412	5,049 ± 1,495	664 ± 421	22.3
E2	912 ± 49	7,507 ± 1,208	6,636 ± 1,430	871 ± 423	25.5
E3	951 ± 64	7,868 ± 1,017	6,881 ± 1,393	987 ± 454	28.3
E4	924 ± 73	6,673 ± 768	5,966 ± 970	706 ± 356	27.2
E-row	913 ± 36	6,940 ± 959	6,133 ±820	807 ± 150	25.8 ± 2.6
Average	847 ± 62	4,561 ± 1,626	4,036 ± 1,429	557 ± 186	25.2 ± 2.0

Supplementary Table 5: Cellular composition of Layer 5 (L5).

	L5-L6 border [µm]	L5 neurons	L5 exc. neurons	L5 inh. neurons	L5 fraction [%]
α	1,158 ± 33	2,856 ± 575	2,323 ± 644	533 ± 202	24.3
β	1,185 ± 35	3,563 ± 194	2,876 ± 389	687 ± 347	23.8
γ	1,247 ± 42	4,706 ± 657	3,758 ± 266	948 ± 402	23.9
δ	1,330 ± 28	5,044 ± 258	3,961 ± 486	1,083 ± 424	23.1
A1	1,191 ± 19	2,968 ± 634	2,427 ± 642	541 ± 185	25.1
A2	1,243 ± 8	2,910 ± 704	2,392 ± 770	519 ± 166	24.3
A3	1,296 ± 40	2,441 ± 292	2,011 ± 399	429 ± 108	25.1
A4	1,313 ± 35	2,554 ± 456	2,027 ± 222	526 ± 272	26.6
A-row	1,261 ± 55	2,718 ± 260	2,214 ± 226	504 ± 51	25.3 ± 1.0
B1	1,239 ± 32	3,357 ± 165	2,690 ± 460	667 ± 301	23.5
B2	1,295 ± 23	3,567 ± 471	2,907 ± 610	660 ± 201	24.6
B3	1,351 ± 42	3,210 ± 554	2,664 ± 658	546 ± 196	24.8
B4	1,368 ± 63	3,220 ± 529	2,620 ± 579	599 ± 189	26.0
B-row	1,314 ± 59	3,338 ± 167	2,720 ± 128	618 ± 57	24.7 ± 1.0
C1	1,285 ± 27	4,098 ± 395	3,360 ± 431	737 ± 279	23.5
C2	1,349 ± 32	4,836 ± 302	3,929 ± 453	907 ± 323	24.6
C3	1,414 ± 34	4,208 ± 453	3,427 ± 570	780 ± 296	24.0
C4	1,429 ± 46	3,591 ± 748	2,955 ± 749	636 ± 206	24.1
C-row	1,369 ± 66	4,183 ± 511	3,418 ± 400	765 ± 112	24.1 ± 0.4
D1	1,373 ± 45	4,607 ± 762	3,764 ± 793	843 ± 271	22.8
D2	1,411 ± 28	5,574 ± 572	4,548 ± 579	1,026 ± 293	23.8
D3	1,451 ± 19	5,325 ± 379	4,277 ± 531	1,048 ± 341	23.6
D4	1,468 ± 55	5,114 ± 315	4,164 ± 304	950 ± 284	23.7
D-row	1,426 ± 42	5,155 ± 411	4,189 ± 326	967 ± 93	23.5 ± 0.4
E1	1,401 ± 30	6,295 ± 619	4,990 ± 678	1,304 ± 374	24.7
E2	1,460 ± 38	6,959 ± 862	5,563 ± 1,020	1,396 ± 413	23.5
E3	1,493 ± 34	6,505 ± 788	5,312 ± 921	1,193 ± 308	23.4
E4	1,464 ± 47	5,877 ± 597	4,751 ± 799	1,125 ± 251	24.0
E-row	1,455 ± 38	6,409 ± 450	5,154 ± 357	1,255 ± 120	23.9 ± 0.6
Average	1,342 ± 98	4,308 ± 1,319	3,487 ± 1,050	820 ± 274	24.2 ± 0.9

Supplementary Table 6: Cellular composition of Layer 6 (L6).

	L6-WM border [µm]	L6 neurons	L6 exc. neurons	L6 inh. neurons	L6 fraction [%]
α	1,612 ± 36	3,238 ± 654	2,903 ± 586	335 ± 79	27.5
β	1,641 ± 58	4,160 ± 421	3,751 ± 328	408 ± 109	27.5
γ	1,746 ± 82	5,411 ± 776	4,928 ± 653	483 ± 132	27.5
δ	1,867 ± 80	6,529 ± 448	5,953 ± 329	575 ± 157	29.9
A1	1,677 ± 33	3,171 ± 570	2,862 ± 564	309 ± 45	26.9
A2	1,760 ± 39	3,195 ± 693	2,895 ± 628	300 ± 86	26.6
A3	1,839 ± 71	2,619 ± 381	2,371 ± 356	248 ± 43	26.8
A4	1,876 ± 57	2,471 ± 663	2,210 ± 592	261 ± 73	25.6
A-row	1,788 ± 88	2,864 ± 373	2,584 ± 346	279 ± 30	26.5 ± 0.6
B1	1,732 ± 56	3,783 ± 327	3,436 ± 290	347 ± 56	26.4
B2	1,830 ± 60	3,563 ± 604	3,209 ± 551	354 ± 80	24.4
B3	1,908 ± 63	3,396 ± 964	3,067 ± 880	328 ± 104	25.8
B4	1,957 ± 76	3,557 ± 767	3,202 ± 722	354 ± 85	28.5
B-row	1,857 ± 98	3,575 ± 159	3,229 ± 153	346 ± 12	26.3 ± 1.7
C1	1,796 ± 73	4,546 ± 658	4,144 ± 588	402 ± 87	26.0
C2	1,892 ± 64	5,215 ± 431	4,718 ± 455	497 ± 77	26.4
C3	1,984 ± 78	4,654 ± 430	4,227 ± 367	427 ± 128	26.5
C4	2,007 ± 63	3,943 ± 1,177	35,51 ± 1,066	391 ± 146	26.1
C-row	1,920 ± 96	4,589 ± 522	4,160 ± 479	429 ± 47	26.3 ± 0.3
D1	1,907 ± 85	5,301 ± 442	4,812 ± 386	489 ± 119	26.5
D2	1,973 ± 44	5,990 ± 349	5,437 ± 250	552 ± 137	25.6
D3	2,037 ± 50	6,099 ± 968	5,517 ± 875	581 ± 162	26.8
D4	2,055 ± 58	5,697 ± 496	5,126 ± 471	571 ± 129	26.4
D-row	1,993 ± 67	5,771 ± 357	5,223 ± 322	548 ± 41	26.3 ± 0.5
E1	1,993 ± 38	7,490 ± 293	6,802 ± 180	688 ± 144	29.5
E2	2,063 ± 50	8,194 ± 1,233	7,421 ± 1,039	773 ± 252	27.7
E3	2,089 ± 15	7,280 ± 2,044	6,587 ± 1,897	692 ± 239	25.7
E4	2,059 ± 61	6,545 ± 1,191	5,903 ± 1,126	642 ± 175	26.5
E-row	2,051 ± 41	7,377 ± 679	6,678 ± 626	699 ± 54	27.4 ± 1.7
Average	1887 ± 141	4,835 ± 1,626	4,376 ± 1,479	459 ± 148	26.8 ± 1.2

Meyer, Egger et al.: The cellular organization of cortical barrel columns is whisker-specific

Supplementary methods: Detection of GAD67-positive somata

September 18, 2013

Contents

Chapter 1

Program flow

1.1 Calculate Brick Dimensions

Images are subdivided into bricks of 1024 x 1024 pixels with an overlap of 5%.

1.2 Statistical Analysis

This step detects bricks containing large amounts of bright pixels, e.g. barrels in L4, which contain a large number of inhibitory synapses around neuron somata. Some parameters in later steps are adjusted for this case to false-positive identification of these somata as GAD67-positive neurons.
For each brick, the histogram of the gray value distribution is computed, normalized to the maximum value and then integrated. Next, the mean m of all bricks in each section is computed. A brick is considered to contain large amounts of bright pixels (called "saturated" from this point on), if the integral of the normalized brick histogram is greater than $a \times m$. Usually, $a = 1$, but this can be adjusted if necessary.

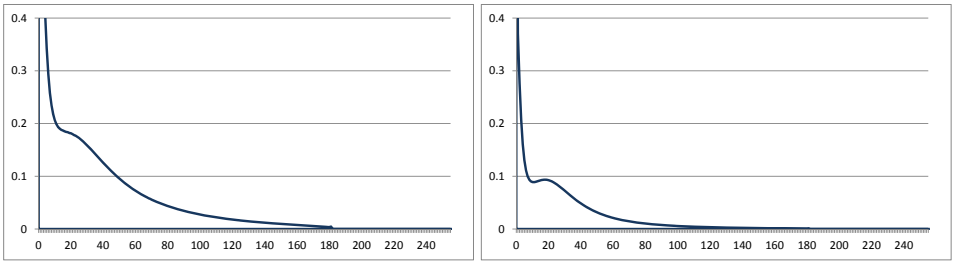

Figure 1.1: Normalized gray value histograms of two bricks within the same image stack.
Left: Saturated brick with histogram integral of 14.5
Right: Unsaturated brick with histogram integral of 6.2

1.3 Preprocessing

The pipeline of filters is illustrated in Figure 1.2.

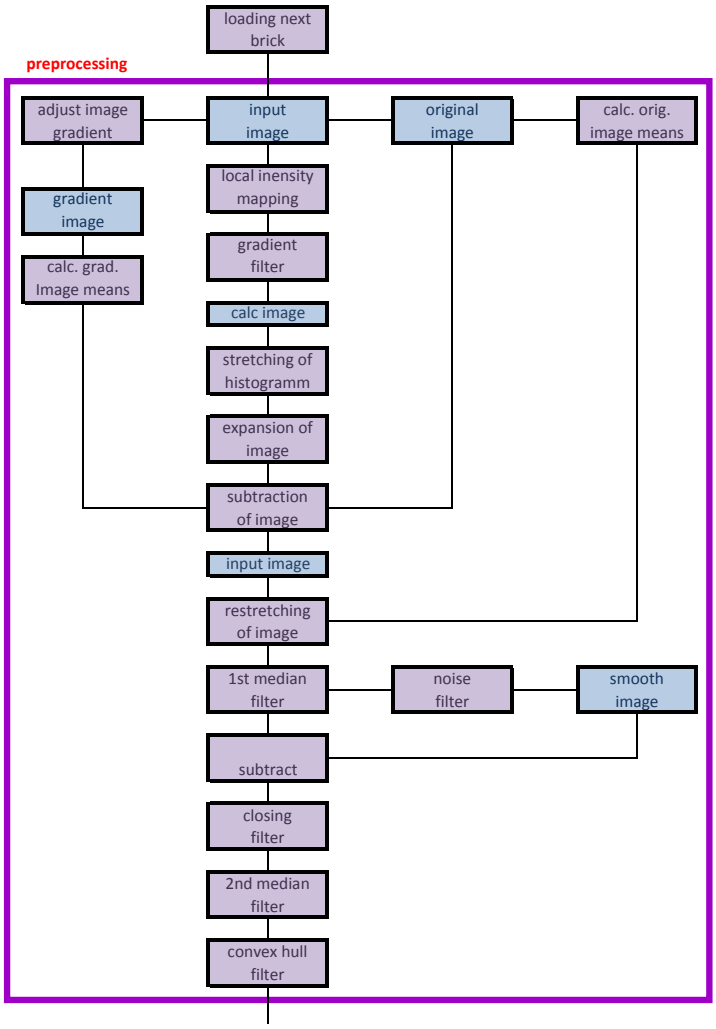

Figure 1.2: Program flow of preprocessing image filters

1.3.1 Compute Background Intensity Gradient

This step compensates for gradients in signal intensity across individual bricks.
For each optical section, a gradient image is computed by subdividing this image into $20 \times 20px$ large areas and computing the mean gray value in circles centered on these low-resolution coordinates (1.3 a). The resulting gray values are normalized to the range from 0 to 255 and interpolated to the full resolution image using Bicubic interpolation (1.3 b).
This pixel-wise background estimate I_{bg} and the mean background $I_{bg,mean}$ of the entire brick are used in the step 1.3.4.

1.3.2 Local Intensity Mapping

In this step, foreground pixel intensities are enhanced by a sigmoidal filter, as described previously (Oberlaender, Dercksen et al., J Neurosci Methods 2009).

1.3.3 Gradient Filter

The gradient magnitude of each optical slice is computed and normalized to a gray value range from 0 to 255. Before this normalization, the 8% of all pixels with the highest gray values are considered as saturated, set to 255 and not considered during calculation of the normalization factor.
Then, all pixel intensities are mapped with an exponential function:

$$I_{exp} = \exp(\gamma \times I_{old})$$

$$\gamma = \frac{\log(255)}{255}$$

1.3.4 Subtraction of Image

For each optical section, the exponential map is subtracted from the original image

$$I_{sub} = I_{original} - W \times I_{exp}$$

Here, the weight W is selected for each pixel individually based on the background intensity gradient and results in more uniform intensity across each optical section:

$$W = \begin{cases} 30 \times \left(\frac{I_{bg} - I_{bg,mean}}{255}\right)^2 & \text{if } I_{bg} > I_{bg,mean} \\ 1 & \text{otherwise} \end{cases}$$

The weight for saturated bricks is computed similarly:

$$W = \begin{cases} 40 \times C_f \left(\frac{I_{bg} - I_{bg,mean}}{255}\right)^2 & \text{if } I_{bg} > I_{bg,mean} \\ 1 & \text{otherwise} \end{cases}$$

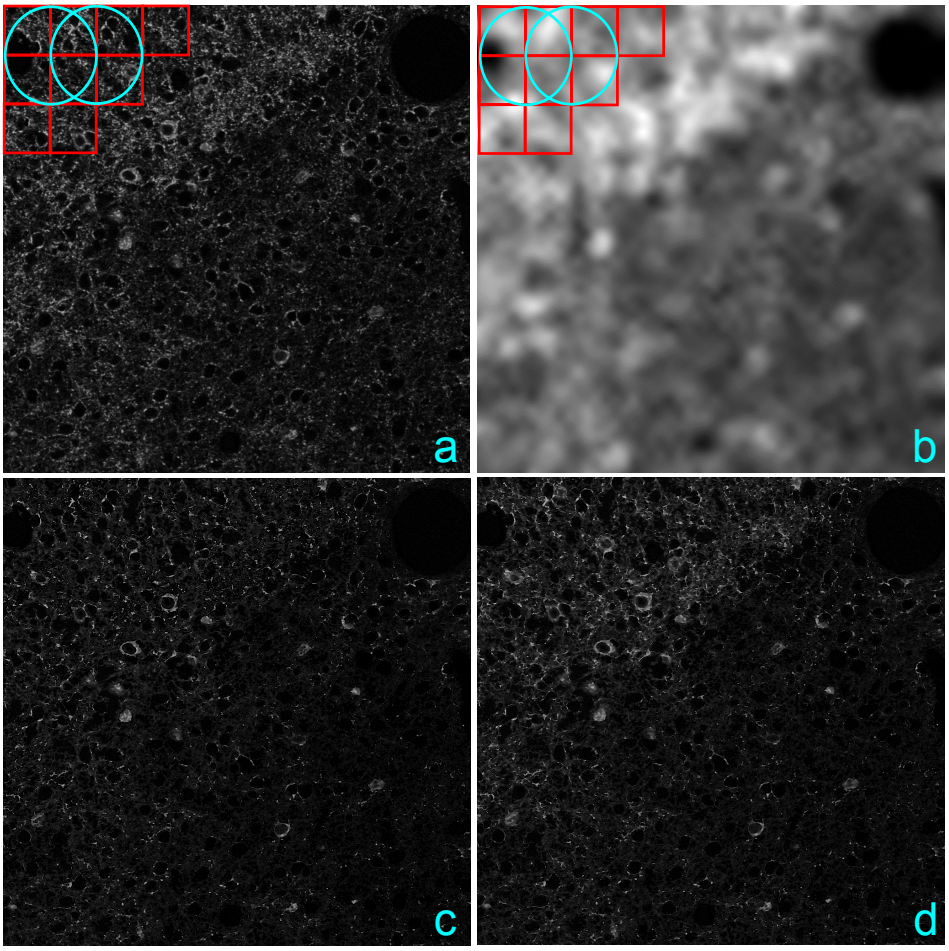

Figure 1.3: a: Image plane with low-resolution coordinates and corresponding circular areas used for calculation of mean gray values.
b: Resulting gradient image
c: Image plane after intensity gradient correction (see step 1.3.4).
d: Image plane without intensity gradient correction. Note higher overall intensity in upper left corner.

Here, C_f is the ratio of the histogram integral of the brick to the histogram integral threshold, as described in 1.2.

1.3.5 Restretching of Image

The gray value range of unsaturated bricks is again normalized from 0 to 255.
Next, for all bricks a lower threshold T is computed from the mean μ_B and standard deviation σ_B of all gray values of this brick.
For unsaturated bricks, the threshold is

$$T = f \times (\mu_B + \sigma_B)$$

For saturated bricks, the threshold is

$$T = f \times \left(\mu_B + \left[1 + \frac{C_f}{12}\right] \times \sigma_B\right)$$

C_f is the ratio of the histogram integral of the brick to the histogram integral threshold, as described previously.

The pixel-wise computed factor f takes varying brightness in individual optical sections into account:

$$f = \begin{cases} 1 + 2 \times \left(\frac{I_{bg} - I_{bg,mean}}{255}\right) & \text{if } I_{bg} > I_{bg,mean} + 1 \\ 1 & \text{otherwise} \end{cases}$$

Pixel gray values in unsaturated bricks are additionally mapped according to

$$I_{new} = I_{old} + \frac{155}{I_{old,MAX}} \times sin^4\left(\frac{\pi}{2} \times \frac{I_{old}}{255}\right)$$

If I_{new} is less than 12, it is set to 0; if I_{new} is greater than 255, it is set to 255.

1.3.6 Median Filter

The image is smoothed and small artifacts are removed with a median filter with a radius of $2px$.

1.3.7 Noise Filter

In this step, the standard deviation I_{STD} in a neighborhood with radius $1px$ around each pixel is computed and mapped according to $I_{border} = (I_{STD})^{1.5}$ and then normalized to an intensity range from 0 to 255.
This image contains mainly the borders of all bright objects.

1.3.8 Subtract

The image containing the borders is now subtracted from the image according to $I_{new} = I_{old} - \frac{1}{2} I_{border}$. Gray values less then 20 are set to 0. This step eliminates small noise objects and reduces medium-sized noise objects in gray value intensity and size.

1.3.9 Closing Filter

Next, a morphological gray scale closing with a radius of $2px$ is applied to the image. This removes small gaps in GAD67-positive neuron somata that may have been introduced in the previous step.

1.3.10 2nd Median Filter

Remaining small artifacts are remove by a second median filter with a radius of $2px$.

1.3.11 Convex Hull Filter

In this step, GAD67-positive somata are reconstructed in 3D. First, each optical section is turned into a binary image by computing all connected components with gray values > 100 and size between 130 and 2,500 pixels. For all remaining connected components, the convex hull is computed, connected by lines with a thickness of $3px$ and unlabeled pixels within the convex hull are labeled as foreground.
This is repeated in order to connect possibly fragmented parts of a single GAD67-positive neuron soma.
Now, for every convex object the number of consecutive optical sections in which this object is present is determined (i.e., the number of optical sections in which convex objects are present which are connected in the z-direction). Objects that occur in less than $S_{min} = 0.06 \times N + 0.8$ sections are discarded as false-positives. Here, N is the total number of optical sections.

The resulting binary objects are split into single neurons as described in (4).

1.4 Delete Clusters with multiple Landmarks

In regions of high GAD67-positive bouton densities, large neuron somata with a high number of perisomatic GAD67-positive boutons may lead to false detection of several small GAD67-positive neuron somata (1.8). In order to correct for this systematic error, all detected GAD67-positive neuron somata are assumed as corresponding to a NeuN-positive neuron soma if the distance between them is less than $20px$. Only if the total size of the NeuN-positive neuron soma is less than $25,000px$, the maximal XY-area of this soma is less than $2,5000px$ and there are at most 2 detected GAD67-positive neuron somata associated with this neuron soma, it is considered a true GAD67-positive neuron soma; otherwise it is deleted.

1.5 Cylindrical Position Correction

Because the convex hull of GAD67-positive neuron somata is computed on individual optical sections, it may occur that a single GAD67-positive neuron is split into 2 or more clusters (1.9). This error is corrected by computing a cylinder with a radius of $6\mu m$ and height of $20\mu m$ around every computed landmark. If there are other landmarks within this volume, they are considered to belong to the same neuron and a new landmark is computed by averaging the 3D positions of the corresponding landmarks.

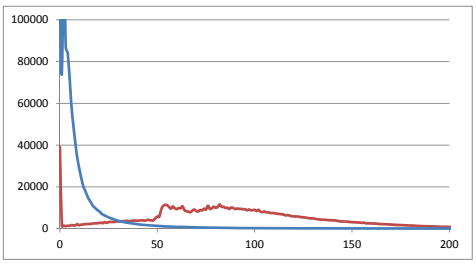

Figure 1.4:
red: gray value histogram of gradient magnitude-filtered image
blue: gray value histogram after normalization and exponential mapping of gray values

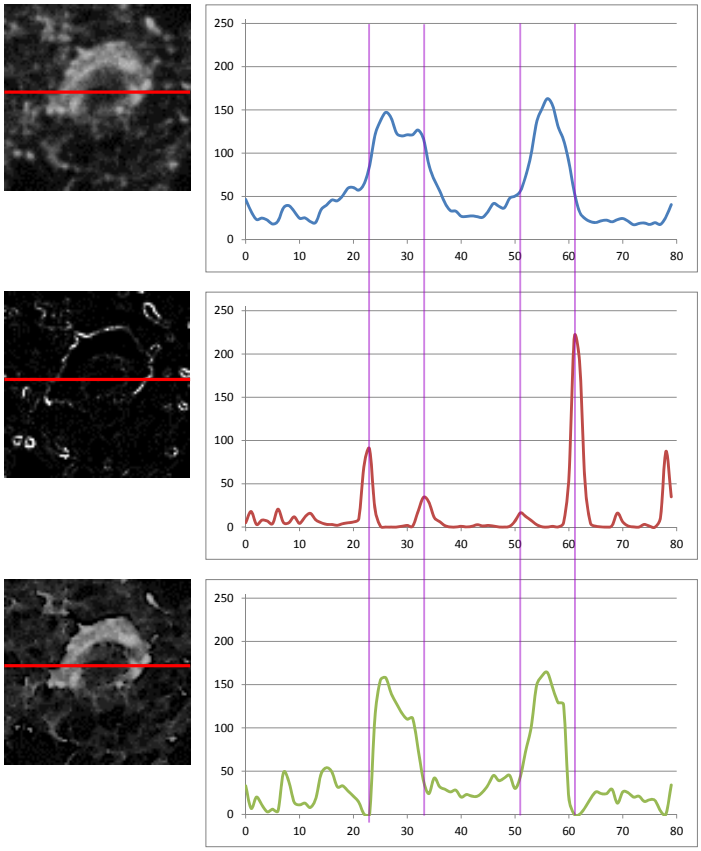

Figure 1.5:
Top: Pixel intensities along the red line across a GAD67-positive neuron soma in the original image.
Center: Pixel intensities along the same line in the gradient-filtered image. Note that only the outline of the GAD67-positive neuron soma and GAD67-labeled boutons are visible.
Bottom: Resulting pixel intensities after subtraction of images (1.2). Note that the GAD67-positive neuron soma is preserved, while small GAD67-positive boutons are removed from the image.

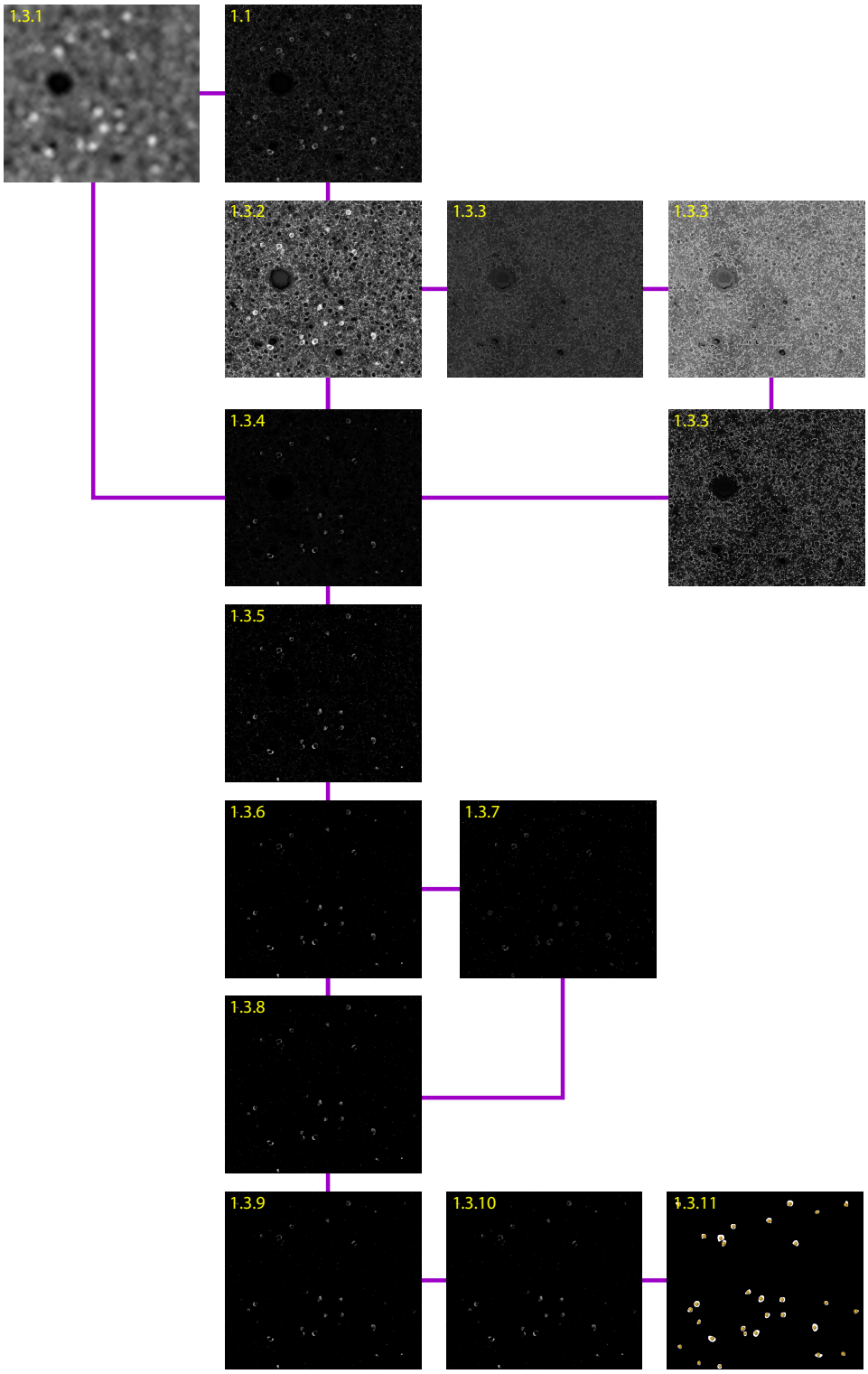

Figure 1.6: Effect of the individual processing steps on one example brick. In the last image, the detected landmarks are added.

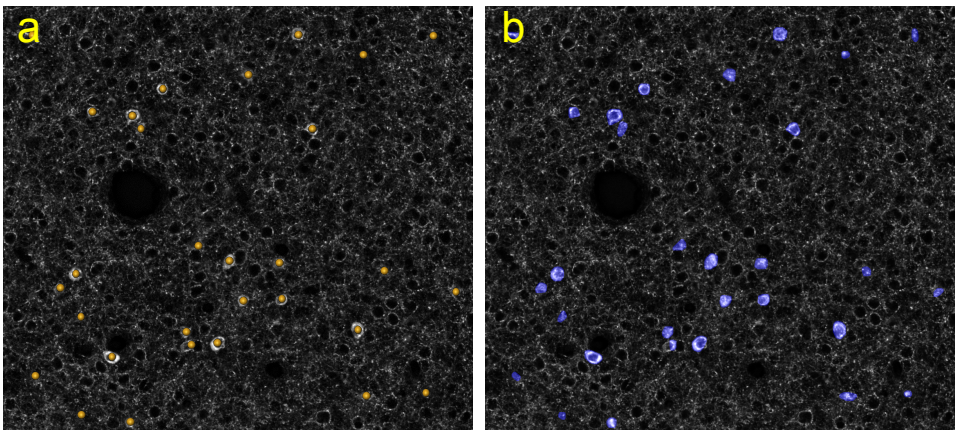

Figure 1.7:
a: original image with final detected landmarks.
b: original image with computed convex hulls.

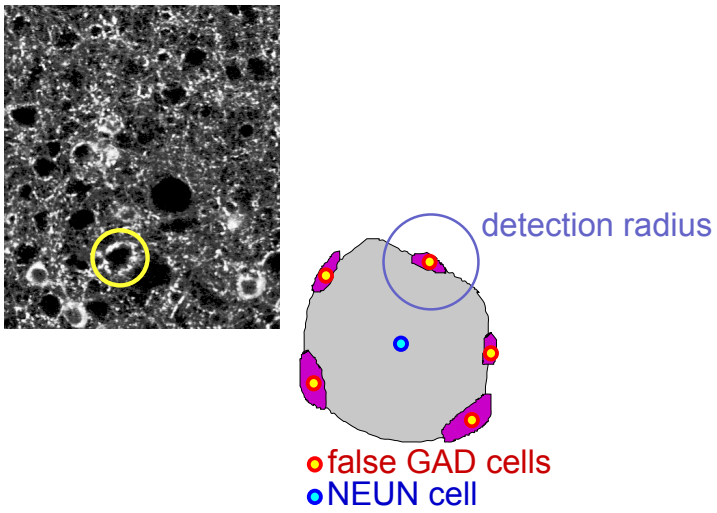

Figure 1.8: Left: Example of a large NeuN-positive, GAD67-negative neuron soma with a large number of perisomatic GAD67-positive boutons (yellow circle). Right: Systematic correction of false-positive GAD67 clusters.

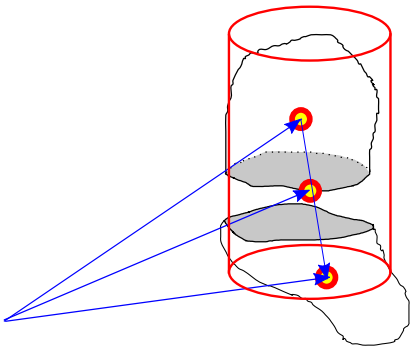

Figure 1.9: Cylindrical Position Correction.

Chapter 2

Validation

2.1 Parameter optimization

All parameters used during preprocessing were systematically tested by comparing the results of the automated detection with manually detected GAD67-positive neuron somata (here, also referred to as somata).
We randomly selected 23 bricks of 1024×1024 pixels size (approx. $370\mu m \times 370\mu m$) from 8 different sections across all cortical layers from one animal. An expert user manually placed landmarks at the locations of all somata. The total number of manually detected somata was 1331, compared with 1303 automatically detected somata. Thus, the relative counting error is 2.2%, similar to previously reported results for NeuN-positive somata (4).
The false-positive (FP) and false-negative (FN) error rates were 32% and 33%, respectively, measured with a correspondence distance of $5\mu m$ (i.e., less than the typical soma size).
We determined the accuracy of the automated soma detection at the typical spatial resolution used in this study by measuring the distance of each automatically detected GAD67-positive soma to the nearest NeuN-positive soma. Then, we counted how many GAD67-positive somata did not have a nearest neighbor within a fixed radius. For radii of $50\mu m$ and $100\mu m$, these values were 12% and 5%, respectively.

2.2 Robustness

To test the robustness of the optimized parameter set, we additionally validated the automated method on manual counts of a nearly complete tangential section (approx. $3mm \times 4mm$). The relative counting error was 3% (total number of somata: 1990), with FP and FN error rates of 22% and 19%, respectively.

2.3 Inter-animal variability

Due to different staining and illumination conditions, we corrected for systematic differences in counting results across the three different animals.
We computed the average vertical density profile for GAD67-positive somata in the C2, D2 and D3 columns. Comparison with results from manual counts of these columns (3) resulted in a depth-dependent correction factor that was applied to the vertical density profile of all columns, taking varying cortical thickness into account.
The average correction factor was 1.46.

Supplementary References

1. Oberlaender M, *et al.* (2012) Cell Type-Specific Three-Dimensional Structure of Thalamocortical Circuits in a Column of Rat Vibrissal Cortex. *Cerebral cortex (New York, NY : 1991).*
2. Meyer HS, *et al.* (2010) Number and laminar distribution of neurons in a thalamocortical projection column of rat vibrissal cortex. *Cereb Cortex* 20(10):2277-2286.
3. Meyer HS, *et al.* (2011) Inhibitory interneurons in a cortical column form hot zones of inhibition in layers 2 and 5A. *Proc Natl Acad Sci U S A* 108(40):16807-16812.
4. Oberlaender M, *et al.* (2009) Automated three-dimensional detection and counting of neuron somata. *J Neurosci Methods* 180(1):147-160.